

# Supplementary Information of “NO<sub>x</sub> Emissions Constraints from GEMS NO<sub>2</sub> Retrievals: Inversion Methodology and Air Quality Model Evaluation in Bangkok using ASIA-AQ Multi-Platform Observations”

Christopoulos et al.

Correspondence to: Julianna Christopoulos (juliechristo@g.ucla.edu)

## S1 Supplementary Methods

### S1.1 Gaussian Plume (GP) Inversion Method

We apply a Gaussian plume model method to estimate NO<sub>x</sub> emissions over Bangkok as outlined in Kuhlmann et al., 2024. This approach fits a vertically integrated Gaussian plume model to GEMS-observed NO<sub>2</sub> column densities, accounting for wind advection, plume dispersion, and chemical loss. The Gaussian plume model for a point source is expressed as:

$$G(x, y) = \frac{QH(x)}{2\sqrt{\pi}u\sigma(x)} \exp\left(-\frac{y^2}{2\sigma(x)^2}\right) + V_{bg}(x, y) \quad (1)$$

$$\sigma(x) = \sqrt{\frac{2Kx^\kappa}{u}} \quad (2)$$

Where  $Q$  is the emission rate,  $u$  is the wind speed,  $H(x)$  is the Heaviside function,  $\sigma(x)$  is the plume width across wind, and  $V_{bg}$  is the background column.  $K$  is the eddy diffusivity coefficient ( $\text{m}^2 \text{s}^{-1}$ ) and  $\kappa$  accounts for nonlinear spreading depending on the meteorological conditions. To obtain values for  $Q$ ,  $K$ ,  $V_{bg}$ , and  $\kappa$ , a least-squares method is used to minimize the cost function:

$$J(Q, K, V_{bg}, \kappa) = \|V_{i,j} - G(x_i, y_i)\|_2^2 \quad (3)$$

Where  $V_{i,j}$  is the observed NO<sub>2</sub> column density for a pixel with center  $(x_i, y_i)$ . Given NO<sub>2</sub>'s short lifetime, it is necessary to multiply the Gaussian plume model by the decay term:

$$D(x, \tau) = H(x) \exp\left(-\frac{x}{u\tau}\right) \quad (4)$$

Where the lifetime,  $\tau$ , is another fitting parameter. Since we are estimating emissions for a city source (Bangkok), the Gaussian model used in this context, accounts for fluxes increasing slowly across the source area. The city emissions are thus described by an emission map,  $p(x, y)$  and a decay term:

$$G_a(x, y) = G(x, y) \int_{-\infty}^{\infty} D(x', \tau) p(x - x', y) dx' \quad (5)$$

The emission map can represent a two-dimensional Gaussian surface  $p(x, y)$ :

$$p(x, y) = \frac{1}{2\pi\sigma_x\sigma_y\sqrt{1-r^2}} \cdot \exp\left(-\frac{(x-x_0)^2}{2\sigma_x^2(1-r^2)} - \frac{(y-y_0)^2}{2\sigma_y^2(1-r^2)} + \frac{r(x-x_0)(y-y_0)}{\sigma_x\sigma_y(1-r^2)}\right) \quad (6)$$

## 31 S1.2 Integrated Mass Enhancement (IME) Inversion Method

32 Lastly, we estimate NO<sub>2</sub> emissions with the Integrated Mass Enhancement (IME) method, which relates the total mass of NO<sub>2</sub>  
 33 observed within the detected plume to the underlying emission rate (Kuhlmann et al., 2024). This method is derived by  
 34 integrating the Gaussian Plume model,  $G(x, y)$ , once the background,  $V_{bg}(x, y)$  is subtracted over a singular polygon:

$$35 \quad M = \int_{y_1}^{y_2} \int_{x_1}^{x_2} G(x, y) - V_{bg}(x, y) dx dy \quad (7)$$

36 Where:

$$37 \quad M = \int_{x_1}^{x_2} \frac{Q}{u} dx \quad (8)$$

$$38 \quad Q = \frac{u}{L} M \quad (9)$$

39 Here,  $u$  is the effective wind speed,  $L = x_2 - x_1$  is the plume length,  $Q$  is the emission rate, and  $M$  is the integrated total mass  
 40 enhancement of the plume.  $M$  in practice is computed as:

$$41 \quad M = \sum_{(i,j) \in \mathcal{P}_a} (V_{i,j} - V_{bg}) \cdot A_{i,j} \quad (10)$$

42 Where  $A_{i,j}$  is the pixel area and  $\mathcal{P}_a$  is the integration area. For NO<sub>2</sub>, a decaying gas, the decay term,  $D(x)$ , is included as well:

$$43 \quad M = \int_{y_1}^{y_2} \int_{x_1}^{x_2} G(x, y) \cdot D(x) dx dy \quad (11)$$

44 The final emission rate,  $Q$ , is determined as:

$$45 \quad Q = \frac{1}{c} \frac{u}{L} M \quad (12)$$

46 where  $c$  is a correction factor that corrects for decay along the plume direction:

$$47 \quad c = \frac{u\tau}{L} \left( \exp\left(-\frac{x_1}{u\tau}\right) - \exp\left(-\frac{x_2}{u\tau}\right) \right) \quad (13)$$

48  
49  
50  
51  
52  
53  
54  
55  
56  
57

58 **S2 Supplementary Figures**

59 **Table S1.** Summary of WRF-Chem D01 validation statistics for Base (B) and Updated (U) simulations against independent  
60 observational datasets. Metrics include mean bias (MB), mean error (ME), normalized mean bias (NMB), normalized mean  
61 error (NME), root-mean-square error (RMSE), and Pearson correlation coefficient (CORR). Details of the evaluation  
62 methodology are provided in Sect. 6.

63

Dataset	Species	Model Run	MB	ME	NMB	NME	RMSE	CORR
GCAS	Tropospheric NO <sub>2</sub> column (molecules cm <sup>-2</sup> )	<b>B</b>	4.0E+15	5.5E+15	91.8	1.3E+2	8.9E+15	0.47
		<b>U</b>	-2.2E+14	2.1E+15	-5.0	49	3.1E+15	0.46
DC-8	NO <sub>x</sub> O <sub>3</sub> NO <sub>2</sub> (ppbV)	<b>B</b>	0.27	0.53	17	33	1.2	0.94
		<b>U</b>	-1.0	1.0	-63	63	1.7	0.94
	CANOE NO <sub>2</sub> (ppbV)	<b>B</b>	0.3	0.57	20.0	36	1.3	0.94
		<b>U</b>	-1.0	1.0	-62	62	1.6	0.9
PCD Ground Monitors	NO <sub>2</sub> (ppbV)	<b>B</b>	6.9	8.2	73	87	11	0.45
		<b>U</b>	-4.6	4.9	-49	53	6.3	0.50
	NO <sub>x</sub> (ppbV)	<b>B</b>	7.1	9.0	68	86	12	0.41
		<b>U</b>	-5.4	5.8	-51	55	7.8	0.57
	O <sub>3</sub> (ppbV)	<b>B</b>	5.2	11.4	17	37	16	0.86
		<b>U</b>	9.0	10.4	29	34	13	0.86
Pandora	Tropospheric NO <sub>2</sub> column (molecules cm <sup>-2</sup> )	<b>B</b>	4.5E+15	9.0E+15	31	62	1.1+16	-0.23
		<b>U</b>	-8.6E+15	8.6E+15	-59	59	1.1E+16	0.23

64

65

66

67

68

69 **Table S2.** Summary of WRF<sub>Base</sub> wind validation statistics against surface observations (Thailand PCD) for 14 – 27 March  
70 2024. Metrics include mean bias (MB), mean error (ME), root-mean-square error (RMSE), and Pearson correlation coefficient  
71 (CORR) included for wind speeds. ERA5 wind speeds align best with ground monitor observations in the BMR.  
72

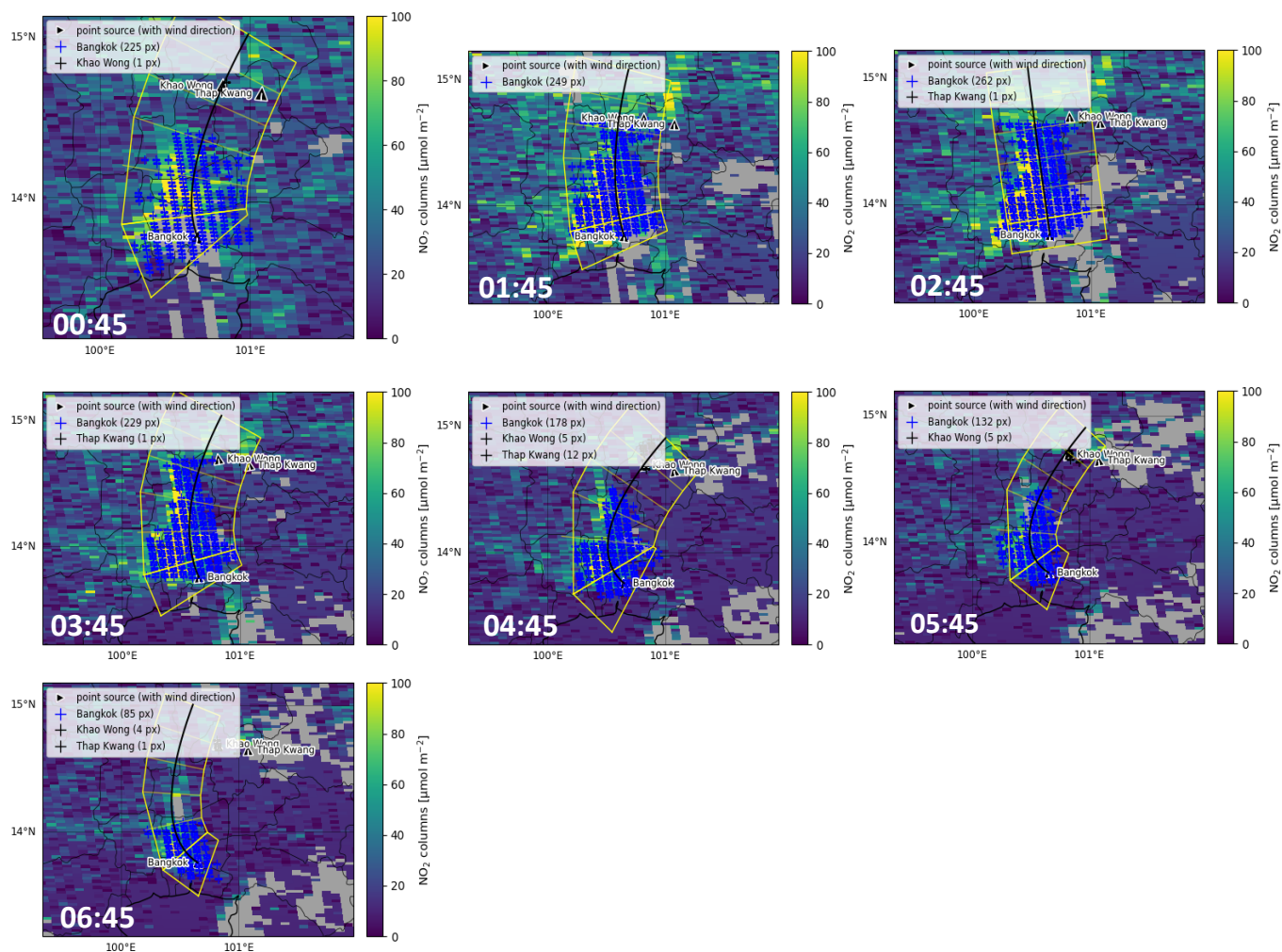
Dataset	Species	Model Run	MB	ME	RMSE	CORR
PCD Ground Monitors	Wind Speed (m s <sup>-1</sup> )	WRF <sub>Base</sub> D02	1.7	1.7	1.9	0.8
		WRF <sub>Base</sub> D01	2.2	2.2	2.6	0.6
		ERA5	1.3	1.4	1.4	0.8
	Wind Direction (°)	WRF <sub>Base</sub> D02	-13	19	24	-
		WRF <sub>Base</sub> D01	7.2	23	32	-
		ERA5	-14	18	21	-

73  
74 **Table S3.** Summary of WRF<sub>Base</sub> PBLH statistics against airborne lidar observations (HSRL-2) for ASIA-AQ flight days,  
75 averaged over raster periods. Metrics include mean bias (MB), mean error (ME), normalized mean bias (NMB), normalized  
76 mean error (NME), root-mean-square error (RMSE), and Pearson correlation coefficient (CORR). Details of the evaluation  
77 methodology are provided in Sect. 6.

78

Date	MB	ME	NMB	NME	RMSE	CORR
18 March	190	420	28	62	590	0.53
19 March	-190	290	-31	48	340	0.27
21 March	330	510	43	67	650	0.31
23 March	150	410	21	56	480	0.54
25 March	190	450	27	63	550	0.72

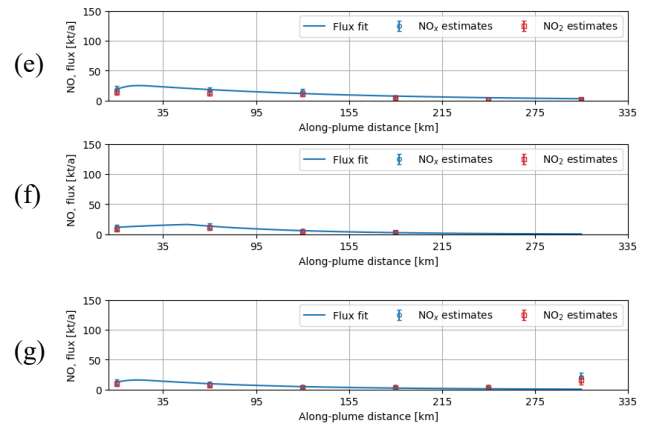
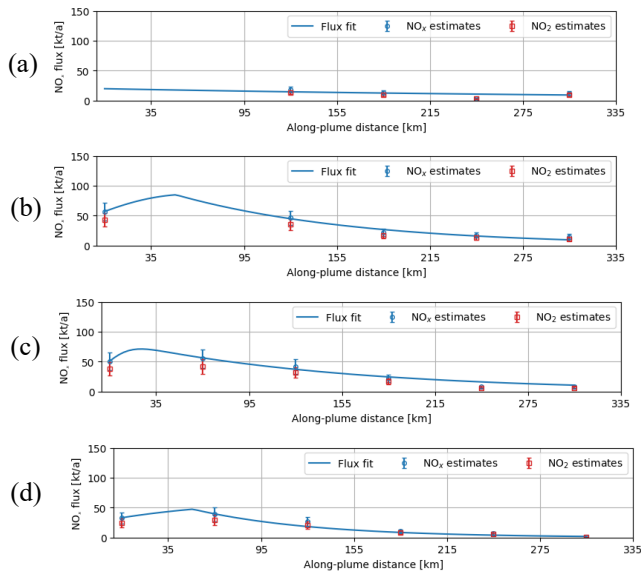
79



81

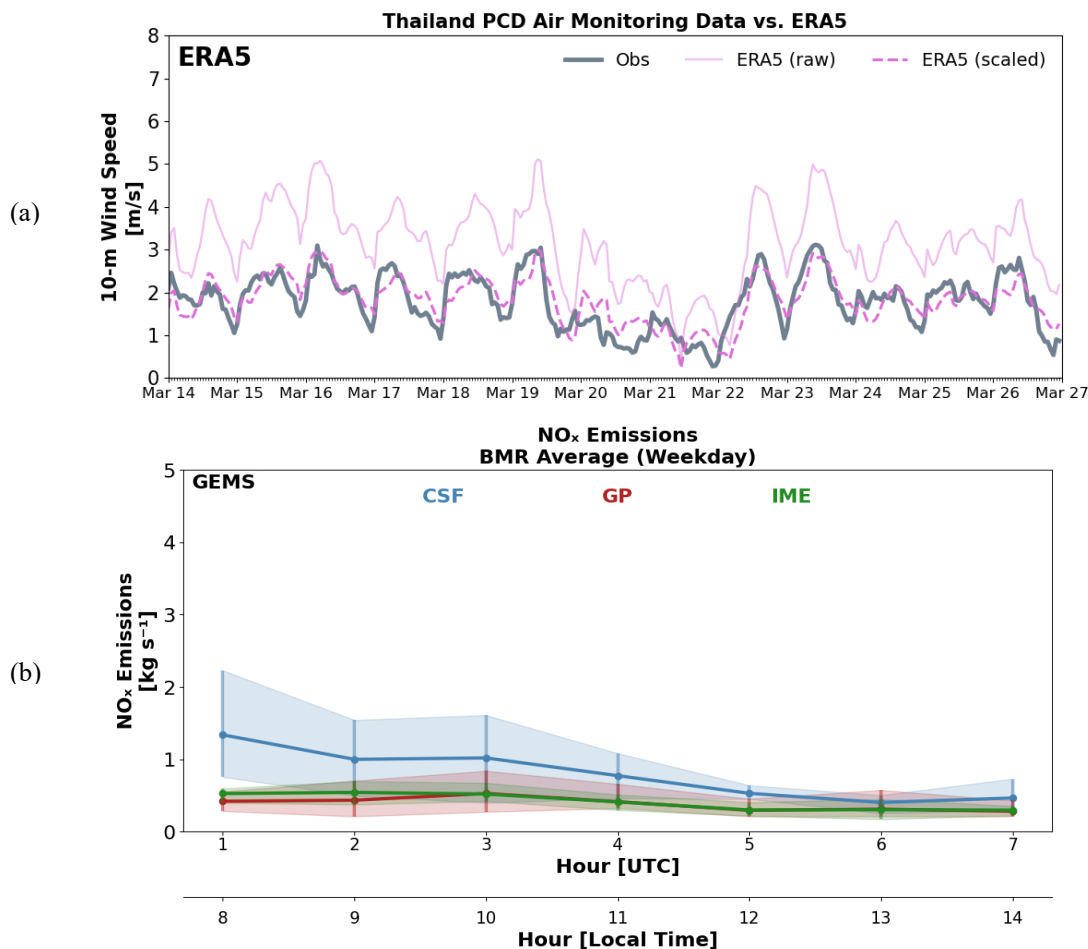
82 **Figure S1.** Example of the cross-sectional flux approach applied on 15 March 2024 using GEMS daytime measurements  
 83 (00:45:00–06:45:00 UTC; 07:45:00–13:45:00 LT), generated with the *ddeq* Python package (Kuhlmann et al., 2024). Detected  
 84 satellite pixels associated with the Bangkok urban plume are marked with blue ticks. A vector originating from Bangkok  
 85 indicates the plume direction based on ERA5 wind fields at the source location. Khao Wong and Thap Kwang districts in  
 86 Saraburi Province represent point sources distinct from the Bangkok urban plume, influenced by limestone quarry operations  
 87 and heavy-truck transport (Makkhao and Prueksasit, 2023).

88



89

90 **Figure S2.** Examples of cross-sectional flux fits on 17 March 2024 for (a) 00:45:00 UTC (07:45:00 LT), (b) 01:45:00 UTC  
 91 (08:45:00 LT), (c) 02:45:00 UTC (09:45:00 LT), (d) 03:45:00 UTC (10:45:00 LT), (e) 04:45:00 UTC (11:45:00 LT), (f)  
 92 05:45:00 UTC (12:45:00 LT), and (g) 06:45:00 UTC (13:45:00 LT), generated with the *ddeg* Python package (Kuhlmann et  
 93 al., 2024). Derived  $\text{NO}_x$  fluxes vary throughout the daytime, with peak values in the morning hours and decreasing toward the  
 94 afternoon, consistent with the daytime pattern of vehicular traffic emissions in the Bangkok Metropolitan Region (BMR).

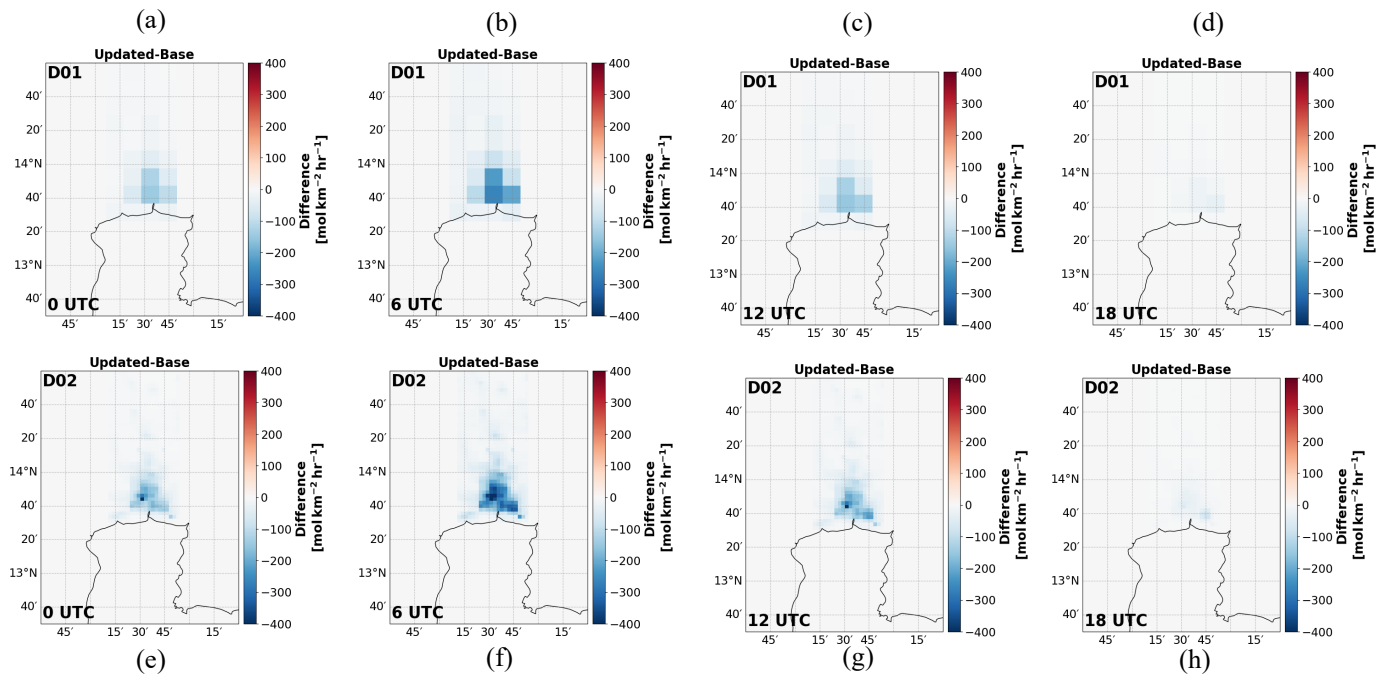


95

96 **Figure S3.** (a) ERA5 (solid pink) and Thailand Pollution Control Department (PCD) ground-monitor network (grey) wind  
 97 speed ( $\text{m s}^{-1}$ ) during the ASIA-AQ deployment period (14–27 March 2024). ERA5 wind speeds scaled by a factor of 0.6 are  
 98 shown as dashed pink lines. (b) GEMS-derived daytime NO<sub>x</sub> emissions ( $\text{kg s}^{-1}$ ) estimated using the cross-sectional flux (blue),  
 99 Gaussian plume inversion (red), and integrated mass enhancement (green) methods. Emissions represent averages across  
 100 daytime hours and weekdays during the ASIA-AQ deployment. As a sensitivity test, ERA5 wind speeds were scaled by a  
 101 factor of 0.6 prior to inversion to assess wind speed uncertainty. Reduced wind speeds lead to lower inferred emissions ( $\approx 40\%$ ),  
 102 consistent with enhanced NO<sub>2</sub> accumulation under weaker transport and a reduced emission flux required to reproduce the  
 103 observed columns. These adjusted emissions fall below those inferred from other observational constraints, suggesting that  
 104 further wind speed reductions may not be appropriate for representing PBL-averaged transport in the BMR.

105

106



107

108 **Figure S4.** Differences in gridded WRF-Chem input emissions (updated – base) expressed in mol km<sup>-2</sup> h<sup>-1</sup> over the Bangkok  
 109 Metropolitan Region (BMR) for D01 at (a) 00:00:00 UTC, (b) 06:00:00 UTC, (c) 12:00:00 UTC, and (d) 18:00:00 UTC, and  
 110 for D02 at (e) 00:00:00 UTC, (f) 06:00:00 UTC, (g) 12:00:00 UTC, and (h) 18:00:00 UTC. The largest differences occur  
 111 during the afternoon local time (e.g., 06:00:00 UTC), reaching up to ~400 mol km<sup>-2</sup> h<sup>-1</sup> in D02.

112

113

114

115

116

117

118

119

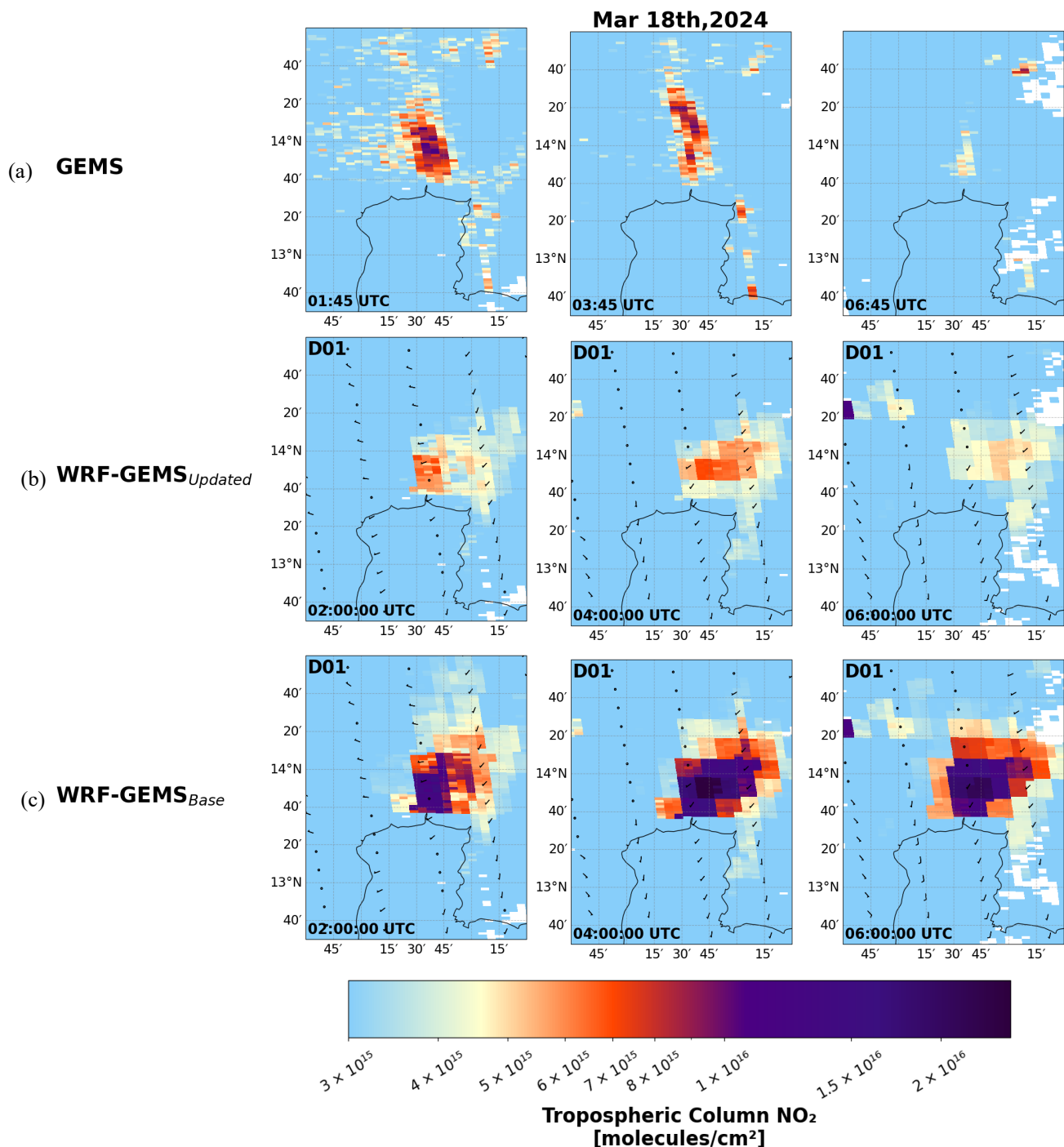
120

121

122

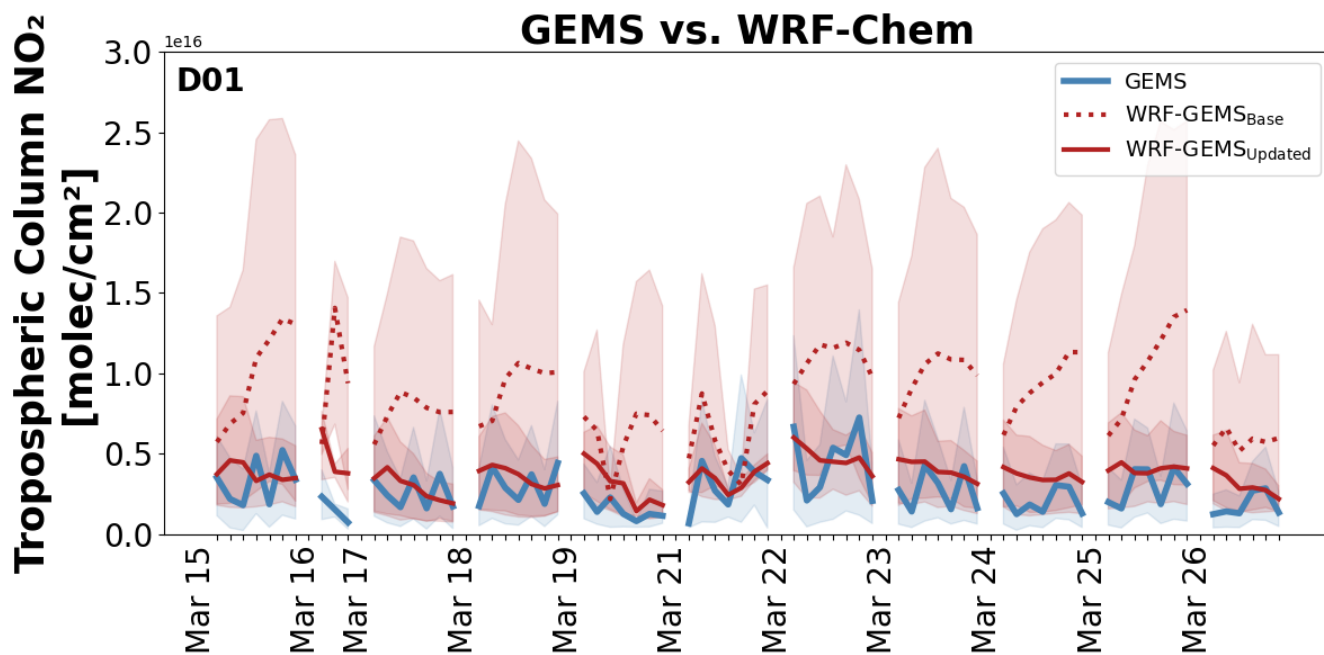
123

124



125

126 **Figure S5.** Spatial comparison over the BMR on 18 March 2024 of tropospheric NO<sub>2</sub> columns from (a) GEMS, (b) WRF-  
 127 GEMS<sub>Updated</sub> D02, and (c) WRF-GEMS<sub>Base</sub> D02 for snapshots at 02:00:00, 04:00:00, and 07:00:00 UTC, corresponding to  
 128 approximately 09:00:00, 11:00:00, and 14:00:00 LT.



130

131 **Figure S6.** Daytime tropospheric NO<sub>2</sub> column comparison between GEMS (blue), WRF-GEMS<sub>Base</sub> D01 (dotted red), and  
 132 WRF-GEMS<sub>Updated</sub> D02 (solid red) during the ASIA-AQ deployment period. Shaded regions indicate variability (10th–90th  
 133 percentiles).

134

135

136

137

138

139

140

141

142

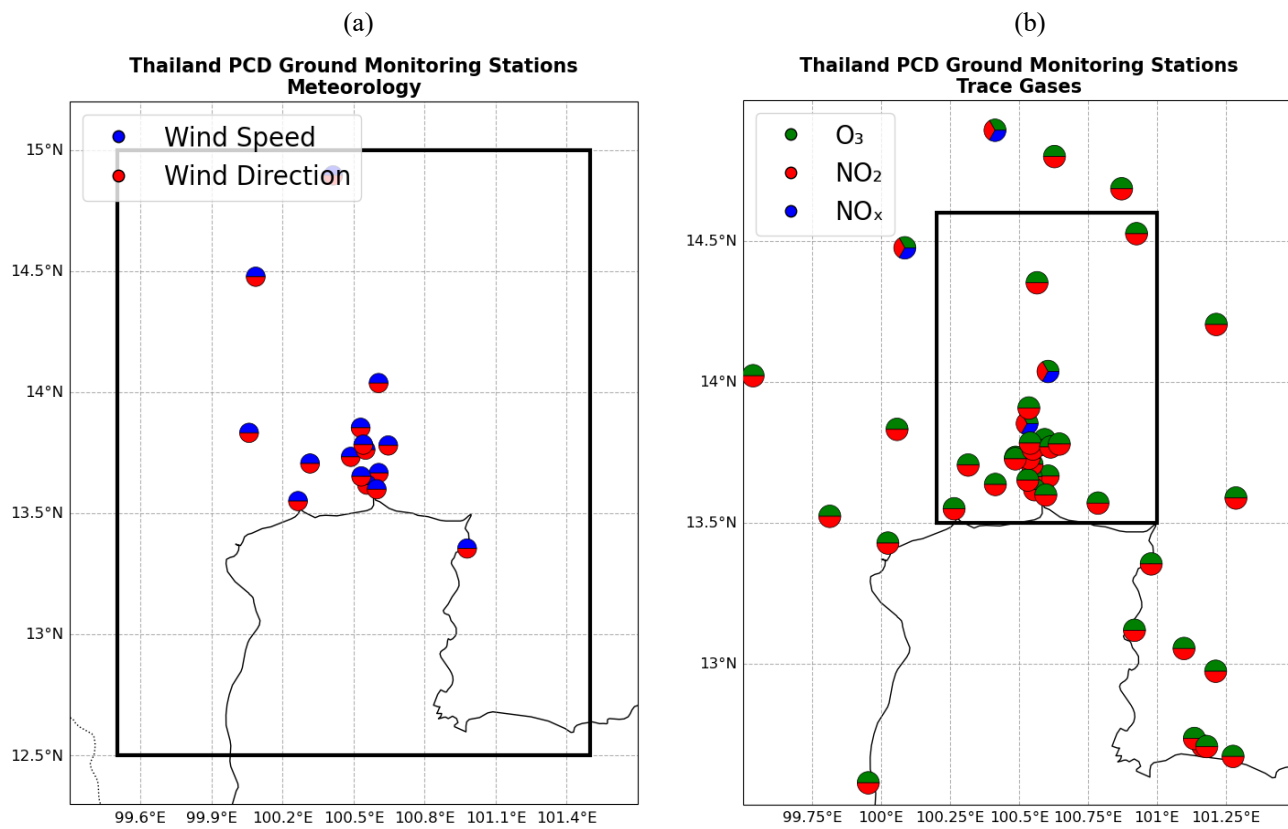
143

144

145

146

147



148

149 **Figure S7.** Locations of Thailand Pollution Control Department (PCD) ground-monitor stations used for evaluation of (a)  
 150 meteorological variables (wind speed and direction) and (b) trace gases ( $\text{NO}_2$ ,  $\text{NO}_x$ ,  $\text{O}_3$ ). Black boxes indicate stations included  
 151 in the analysis. For trace gas evaluation, stations within the Bangkok urban plume were selected to assess the region where the  
 152 inversion was applied, whereas meteorological evaluation includes a broader regional domain to better capture spatial  
 153 variability in winds.

154

155

156

157

158

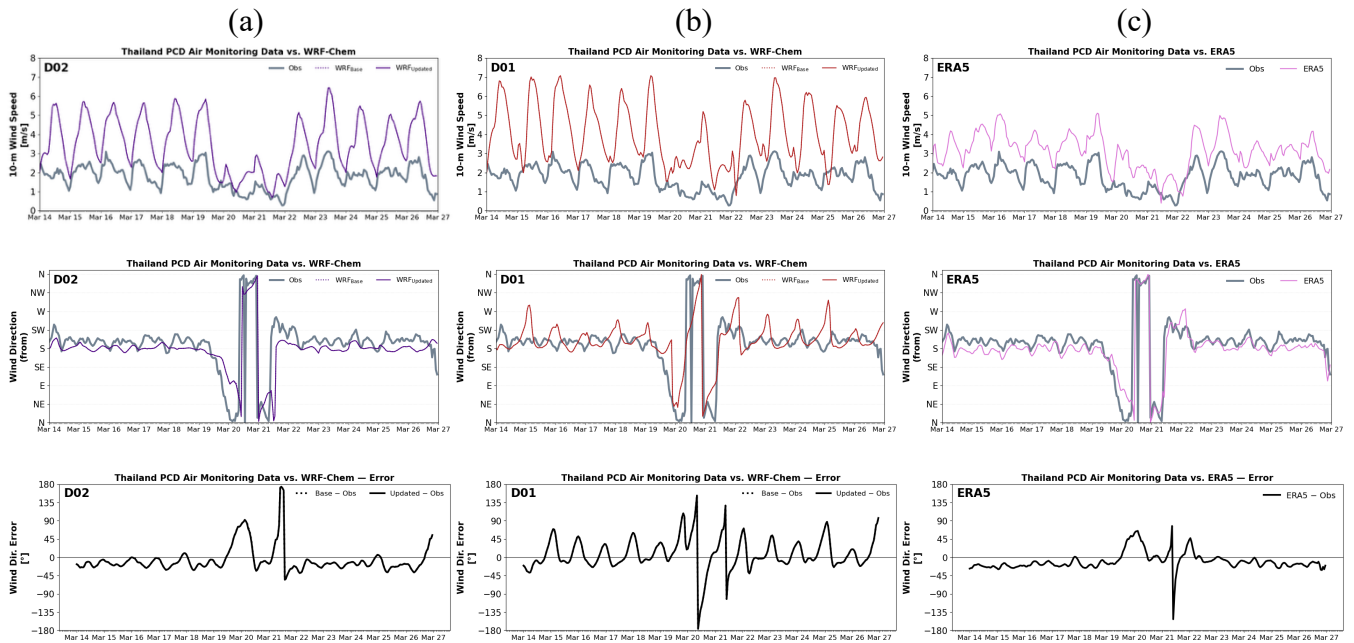
159

160

161

162

163



164

165

166

167

168

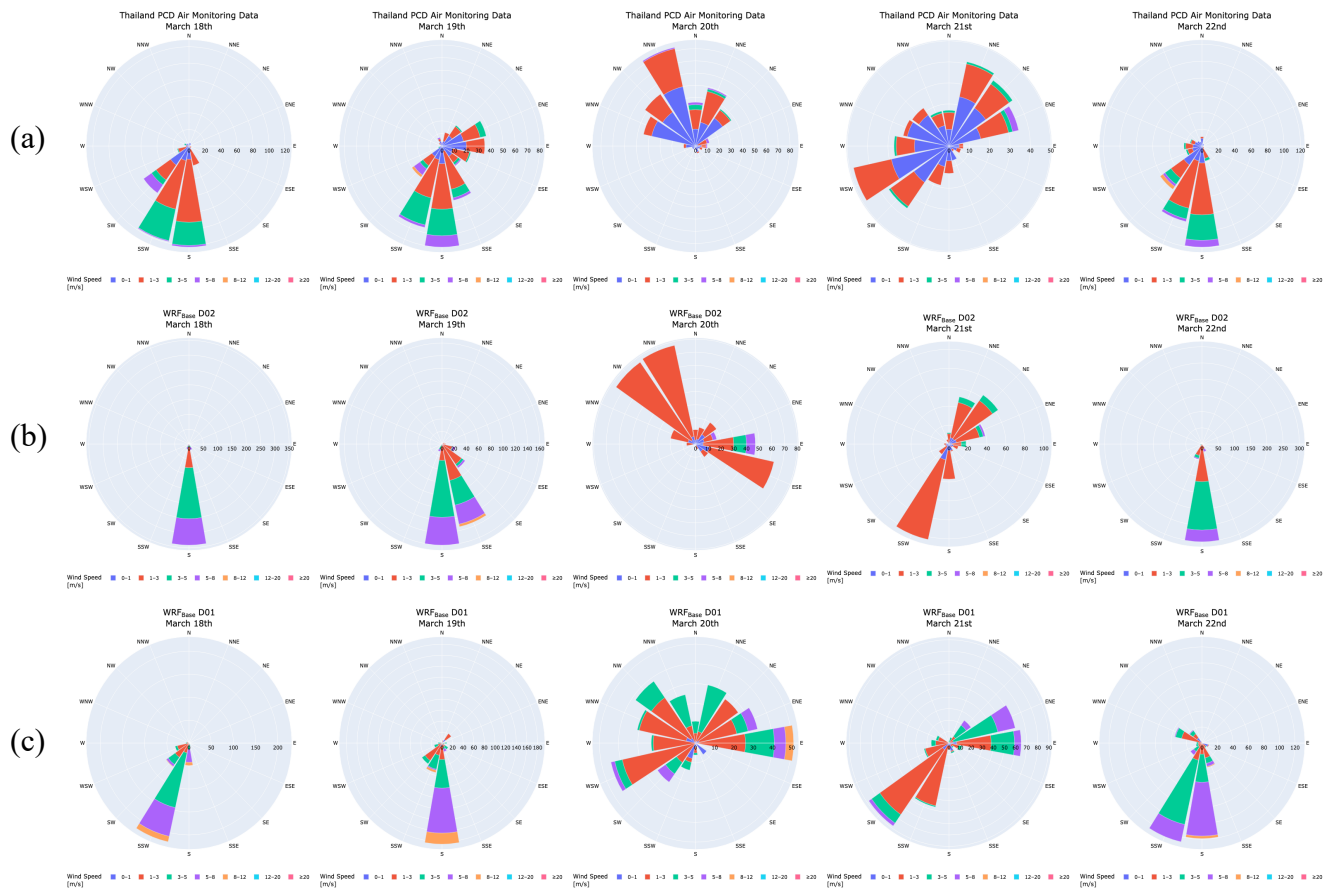
169

170

171

172

**Figure S8.** Comparison of (a) WRF<sub>Base</sub> D02 (purple), (b) WRF<sub>Base</sub> D01 (red), (c) ERA5 (pink) to Thailand Pollution Control Department (PCD) ground-monitor network (grey) wind speed ( $\text{m s}^{-1}$ ), wind direction (from), and wind direction error during the ASIA-AQ deployment period (14–27 March 2024). Lines represent averages across stations within the BMR and surrounding regions. Both model domains and ERA5 overestimate wind speeds relative to surface observations, potentially due to unresolved urban canopy effects. These results suggest that improved urban parameterizations (e.g., a multi-layer urban canopy model) could enhance model performance. Error diagnostics also highlight misrepresentation of a short-lived northeasterly wind event on 20–21 March, leading to temporary errors in simulated transport direction.



174

175 **Figure S9.** Comparison of observed wind roses (a) with modelled wind roses from (b) WRF<sub>Base</sub> D02 and (c) WRF<sub>Base</sub> D01  
 176 over the BMR for 18–22 March 2024. Panels show the frequency distribution of wind speed and direction. While the model  
 177 captures the dominant southerly flow, wind speeds are consistently overpredicted in both domains. The largest discrepancies  
 178 occur on 20–21 March, when the model fails to capture the observed shift toward northeasterly winds, likely contributing to  
 179 transport and concentration errors during this period.

180

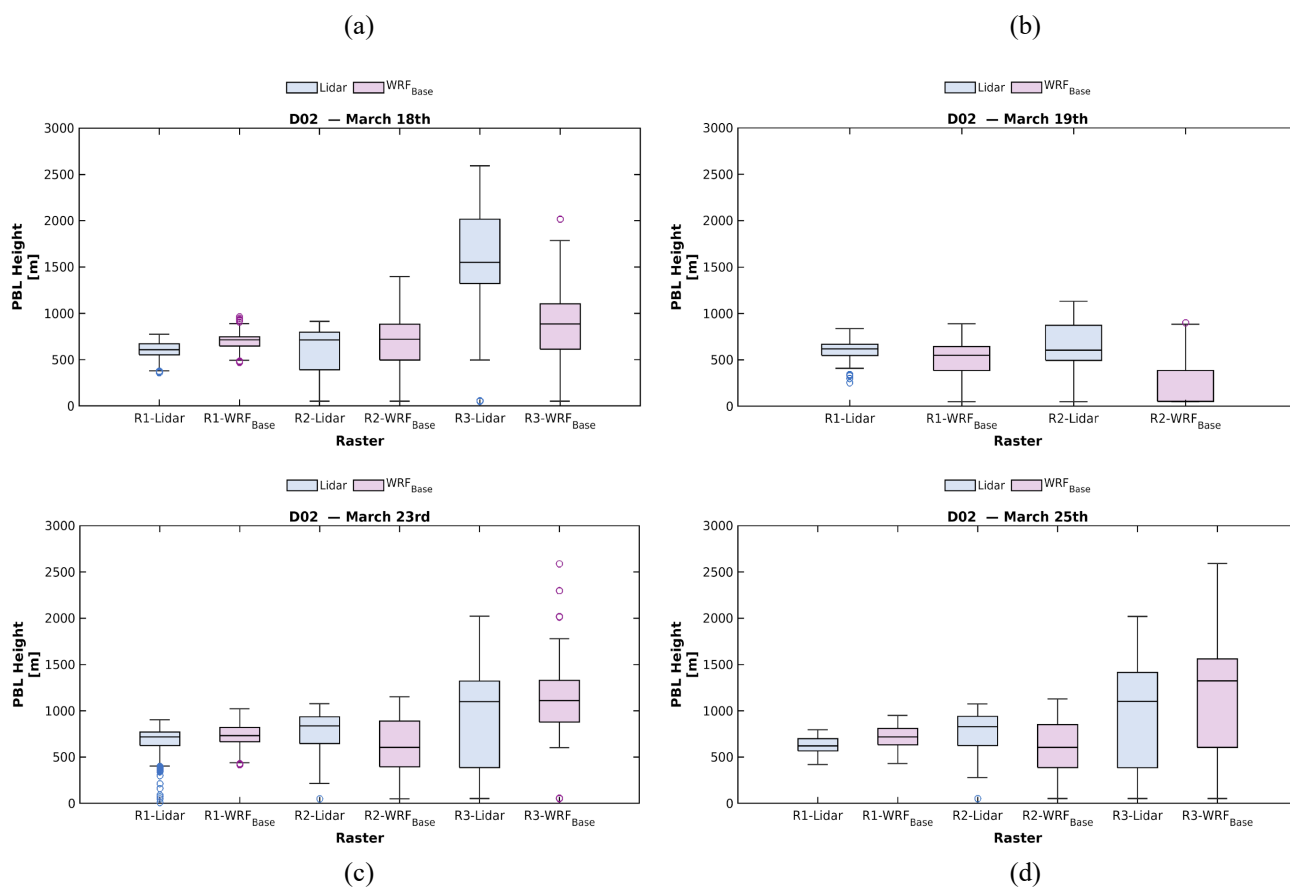
181

182

183

184

185



187

188 **Figure S10.** Evaluation of observed lidar-derived (blue) and modelled WRF<sub>Base</sub> D02 (magenta) planetary boundary layer height  
 189 (PBLH; m) for ASIA-AQ flight days on (a) 18 March, (b) 19 March, (c) 23 March, and (d) 25 March 2024. PBLH was derived  
 190 from airborne HSRL-2 lidar observations following the methodology of Christopoulos et al. (2025). Overall, WRF-Chem  
 191 reproduces the temporal evolution of the daytime boundary layer reasonably well on several days ( $CORR = 0.5-0.7$ ),  
 192 particularly during periods of strong convective mixing. However, the model exhibits biases in PBL depth. These results  
 193 suggest that while WRF reasonably captures the timing of PBL evolution, it frequently misrepresents the magnitude of  
 194 boundary layer development, particularly over-deepening the PBL during rapid daytime growth.

195

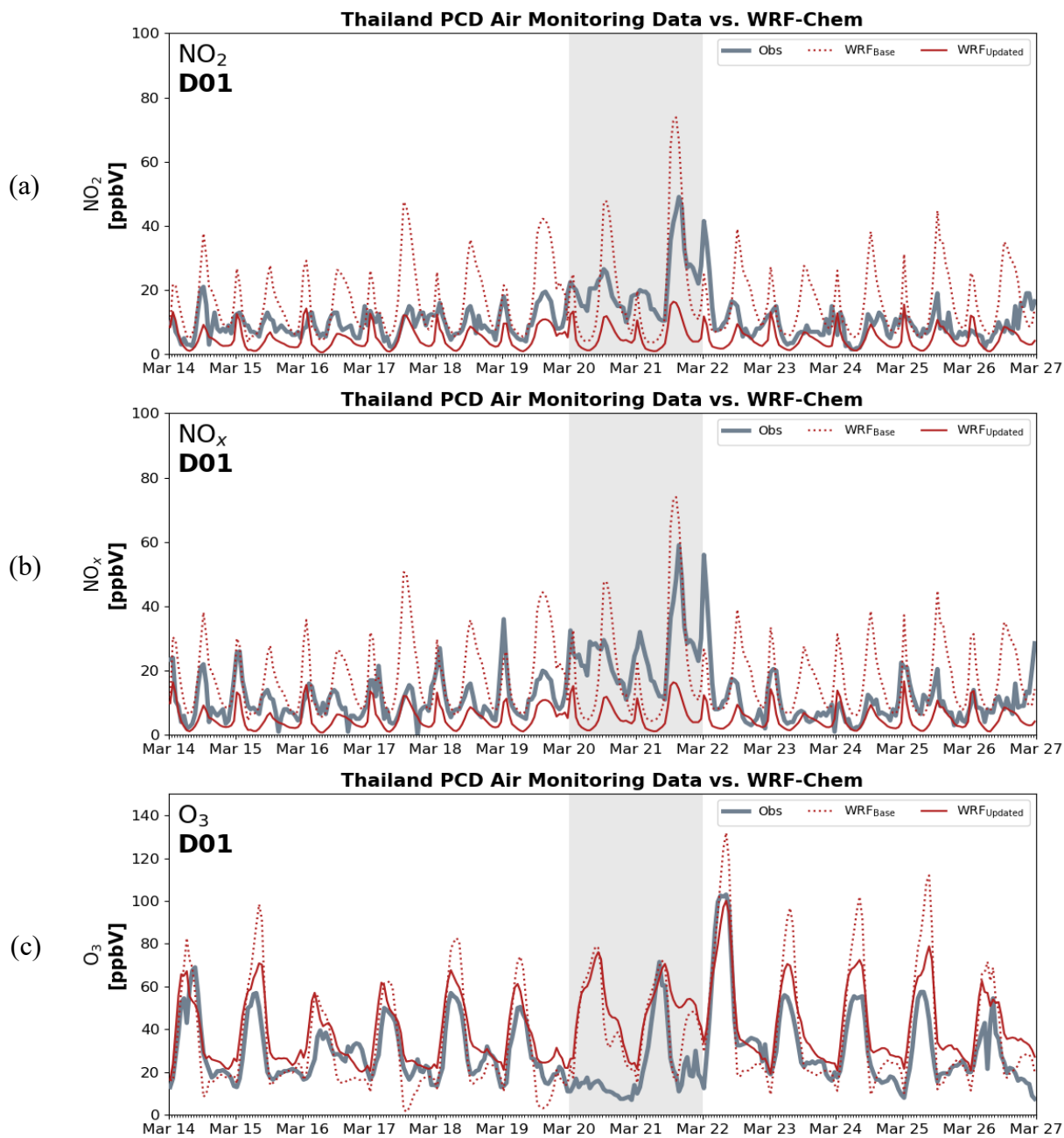
196

197

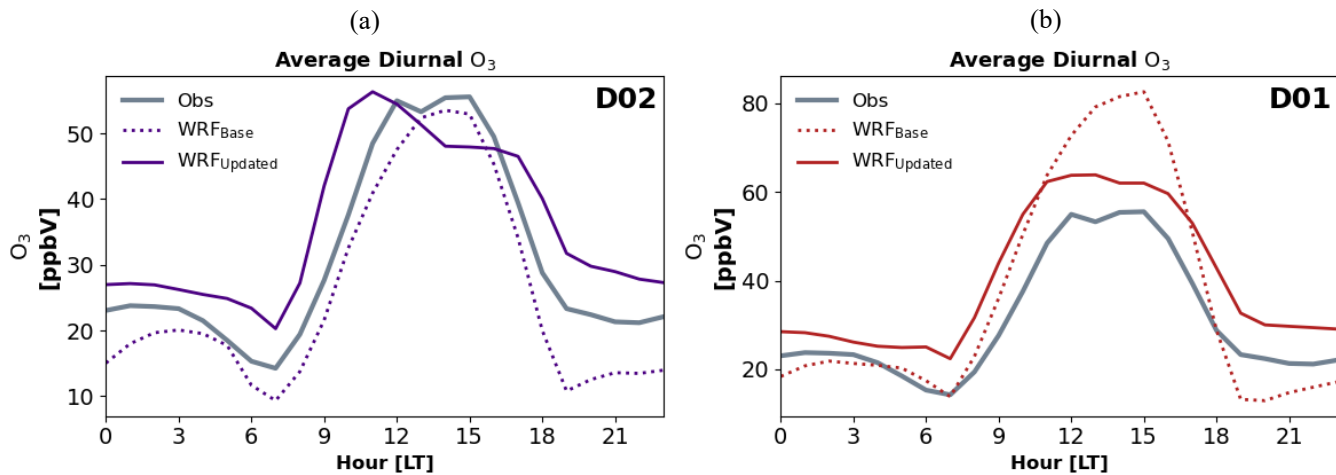
198

199

200



201  
 202 **Figure S11.** Comparison of WRF<sub>Base</sub> D01 (dotted red) and WRF<sub>Updated</sub> D01 (solid red) simulations against Thailand Pollution  
 203 Control Department (PCD) ground-monitor network observations for (a) NO<sub>2</sub> mixing ratio (ppbv), (b) NO<sub>x</sub> mixing ratio (ppbv),  
 204 and (c) O<sub>3</sub> mixing ratio (ppbv) during the ASIA-AQ deployment period (14–27 March 2024). Lines represent averages across  
 205 stations within the Bangkok urban plume.



206

207 **Figure S12.** Average diurnal cycles of O<sub>3</sub> for (a) D01 and (b) D02 comparing WRF<sub>Base</sub> (dotted) and WRF<sub>Updated</sub> simulations  
 208 against Thailand Pollution Control Department (PCD) ground-monitor network observations during the ASIA-AQ deployment  
 209 period (14–27 March 2024).

210

211

212

213

214

215

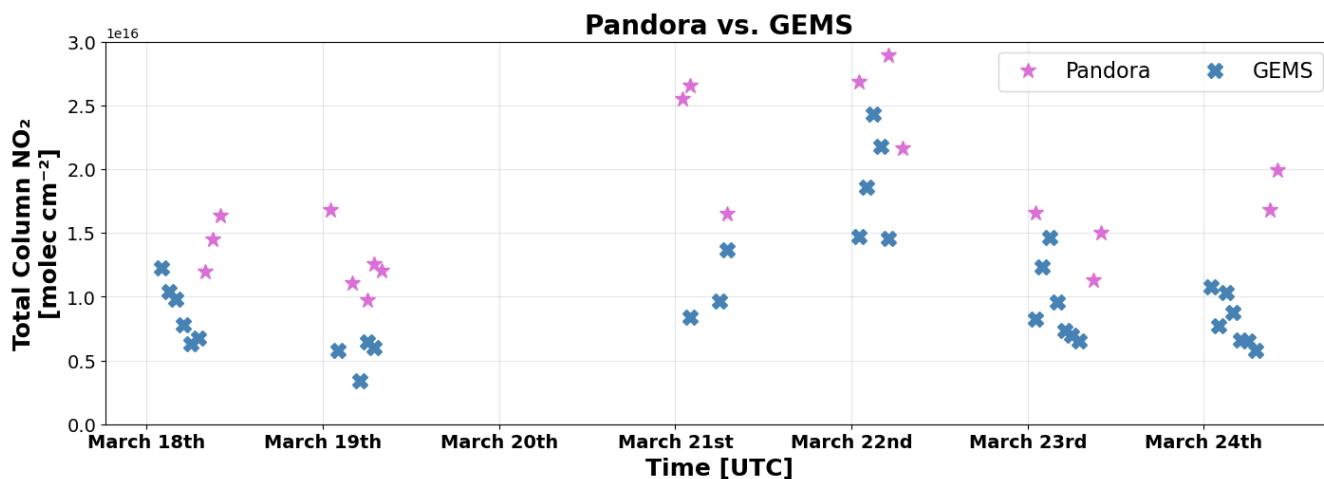
216

217

218

219

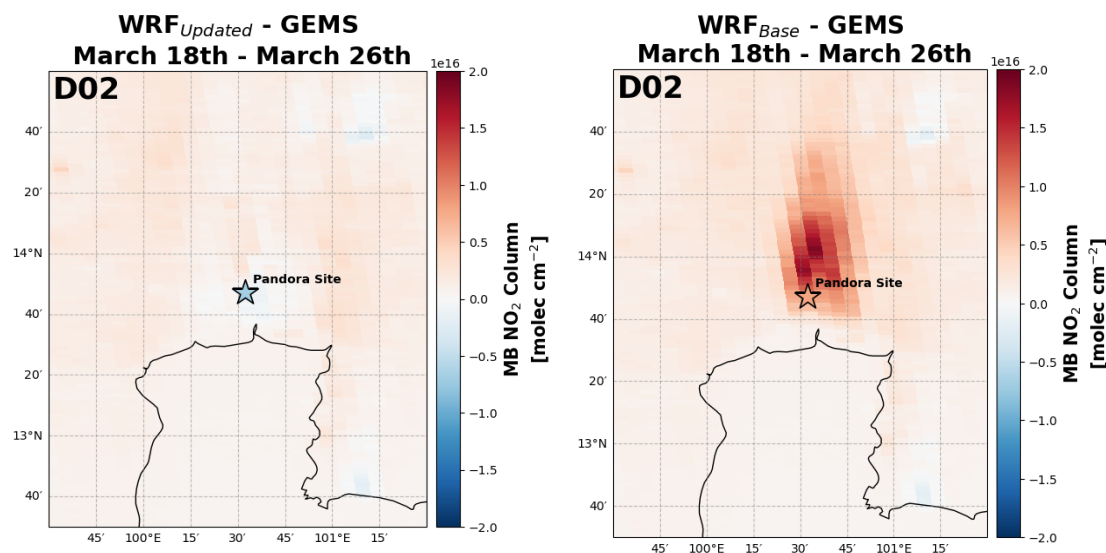
220



221

222 **Figure S13.** Comparison of Pandora (pink) and GEMS (blue) total column NO<sub>2</sub> for high-quality observations during the ASIA-  
 223 AQ deployment period. GEMS reproduces the temporal variability observed by Pandora (CORR = 0.7) but systematically  
 224 underestimates column magnitudes (mean bias  $\approx -9.2 \times 10^{15}$  molecules cm<sup>-2</sup>), with the largest discrepancies occurring during  
 225 the stagnation event on 21 March 2024.

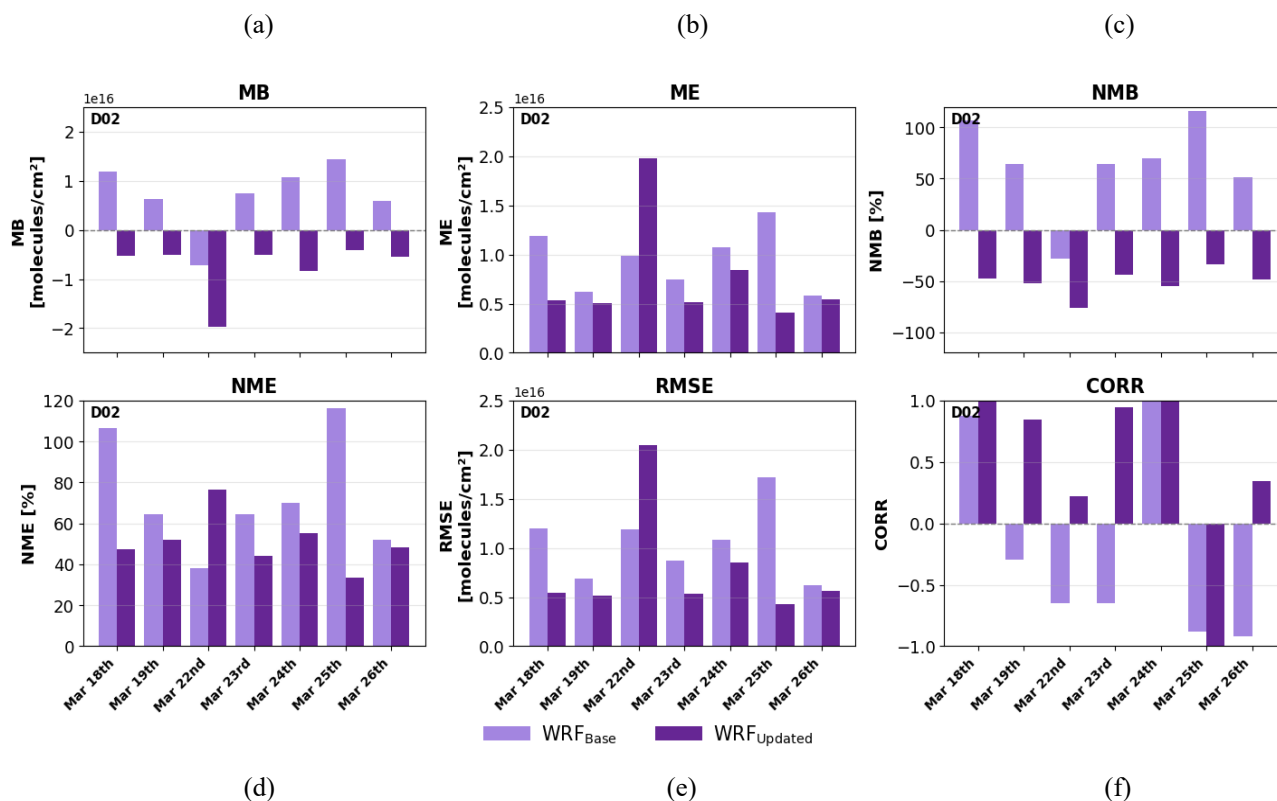
226



227

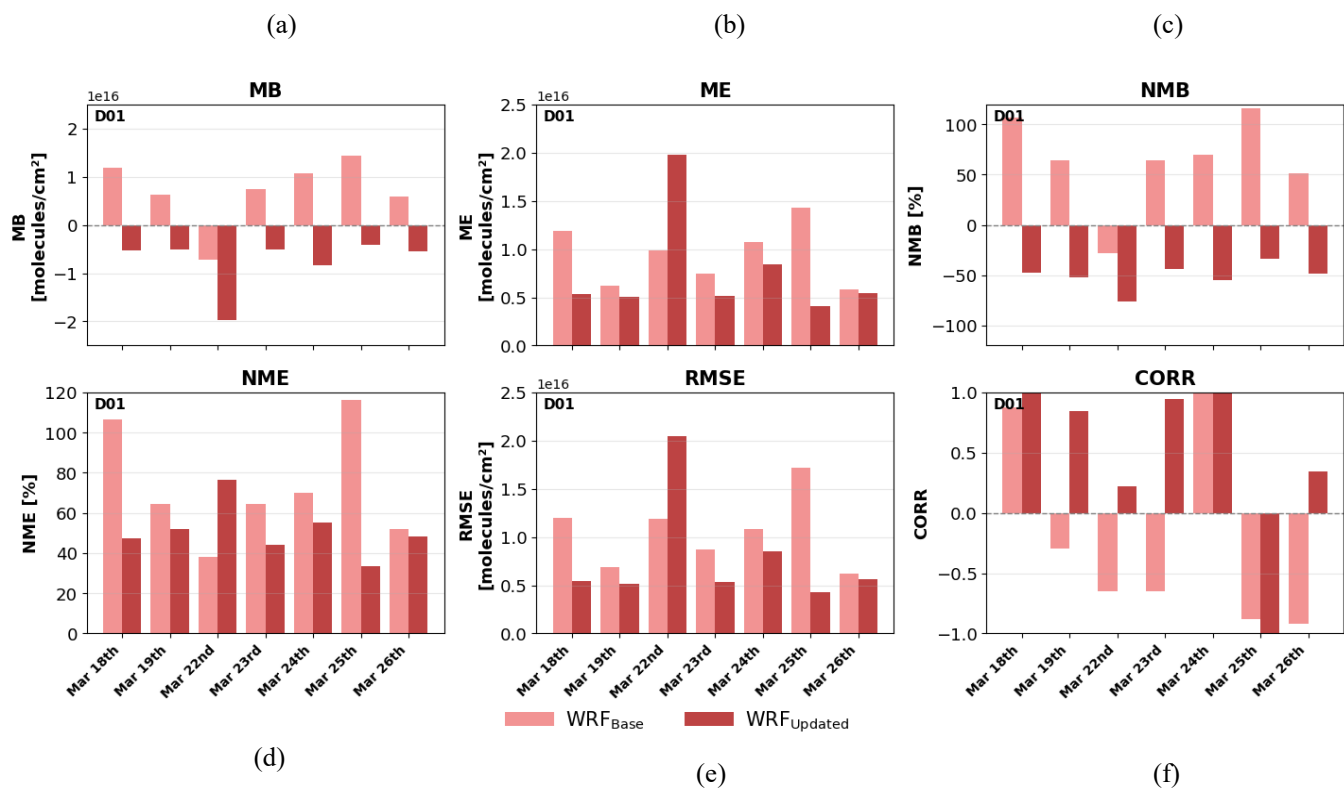
228 **Figure S14.** Spatial distribution of mean NO<sub>2</sub> column bias over the BMR averaged over 18–26 March 2024. Background  
 229 shading represents WRF–GEMS bias, with the Pandora site location and corresponding model bias indicated. Results are  
 230 shown for (a) WRF<sub>Updated</sub> and (b) WRF<sub>Base</sub> simulations.

231



232  
 233  
 234  
 235  
 236  
 237  
 238  
 239  
 240  
 241  
 242  
 243

**Figure S15.** Statistical performance metrics for WRF<sub>Base</sub> D02 (light purple) and WRF<sub>Updated</sub> D02 (dark purple) evaluated against Pandora observations during the ASIA-AQ deployment period (14–27 March 2024). Only days with high-quality Pandora data were included. Metrics include (a) mean bias (MB), (b) mean error (ME), (c) normalized mean bias (NMB), (d) normalized mean error (NME), (e) root-mean-square error (RMSE), and (f) correlation coefficient (CORR).



244

245 **Figure S16.** Same as Figure S13, but for WRF<sub>Base</sub> D01 (light red) and WRF<sub>Updated</sub> D01 (dark red) evaluated against Pandora  
 246 observations during the ASIA-AQ deployment period (14–27 March 2024).

247

248

249

250

251

252

253

254

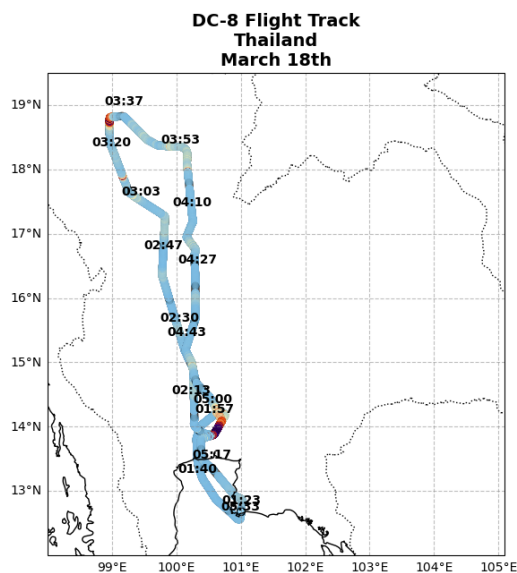
255

256

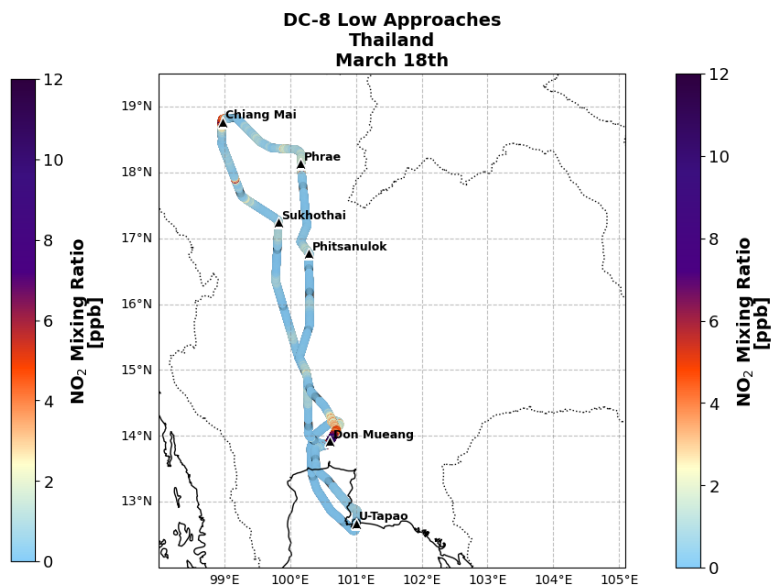
257

258

(a)



(b)



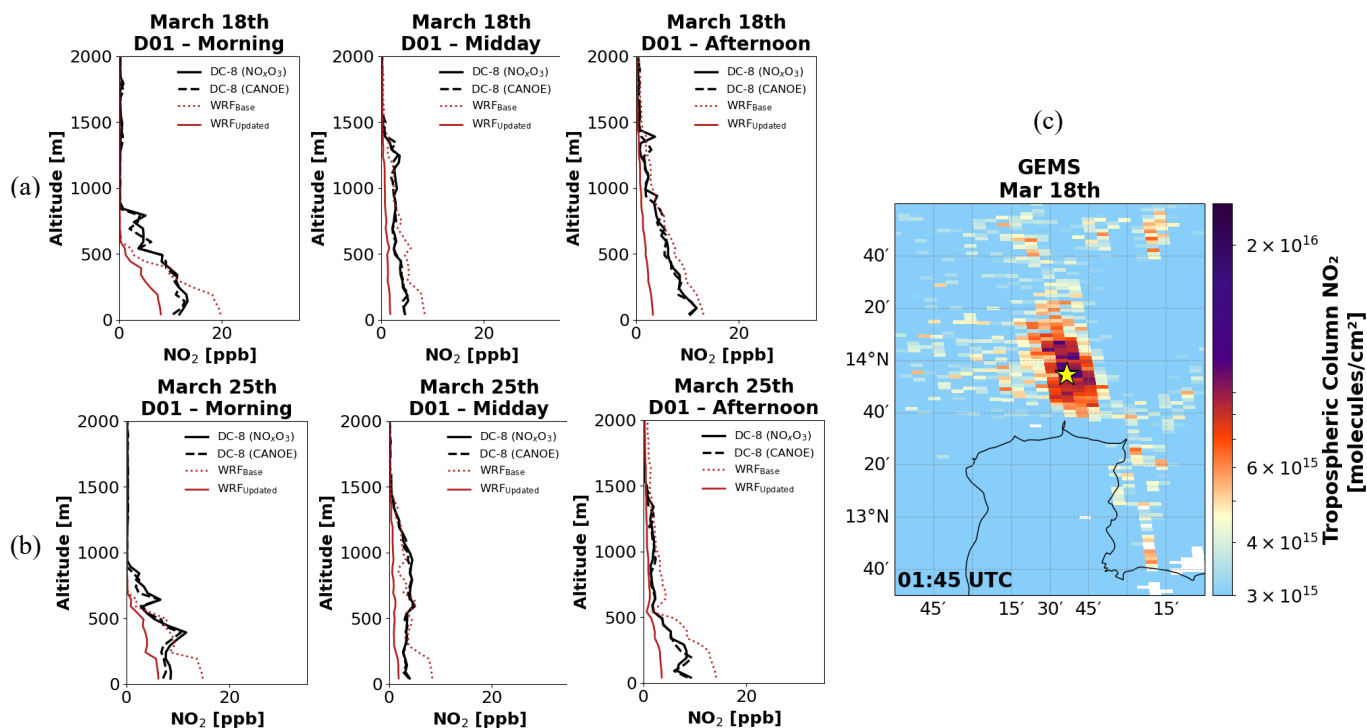
259

260 **Figure S17.** (a) Typical DC-8 flight track during the Thailand-led ASIA-AQ field campaign. The aircraft departed from U-  
 261 Tapao Rayong Pattaya International Airport and flew northward across Bangkok and central Thailand toward Chiang Mai.

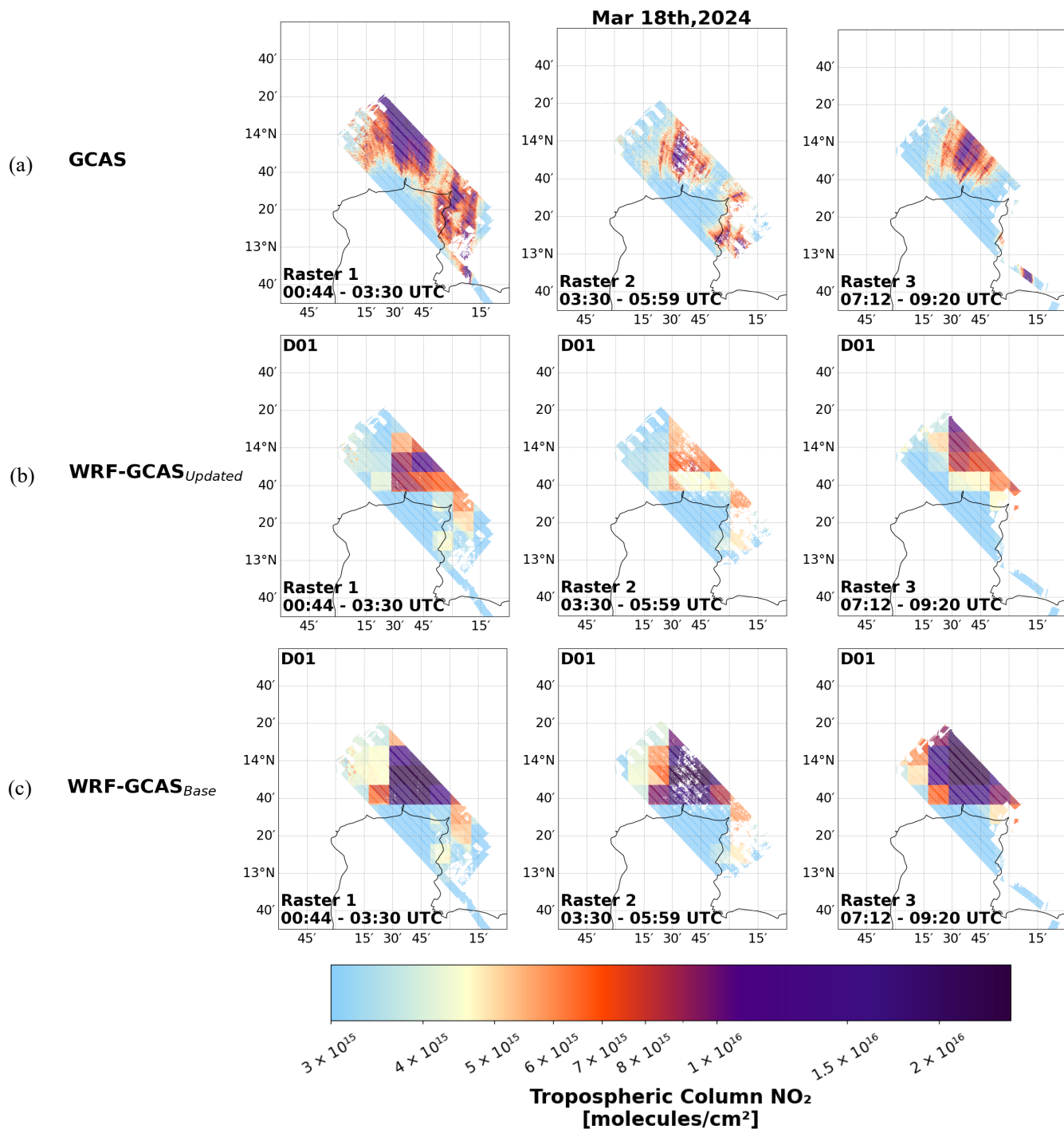
262 (b) Locations of airports where the DC-8 conducted low approaches for profiling and sampling surface air quality (U-Tapao,  
 263 Don Mueang, Phitsanulok, Sukhothai, Phrae, and Chiang Mai).  $\text{NO}_2$  mixing ratios (ppbv) measured by NCAR's  $\text{NO}_x\text{O}_3$

264 instrument are shown along the flight track, with time annotations indicated.

265



266  
 267 **Figure S18.** Comparison of WRF-Chem D01 simulations (WRF<sub>Base</sub>: dotted red; WRF<sub>Updated</sub>: solid red) with airborne in situ  
 268 measurements from the CANOE (dashed black) and NO<sub>x</sub>O<sub>3</sub> (solid black) instruments aboard the DC-8 for (a) 18 March and  
 269 (b) 25 March 2024. Profiles are grouped by morning (06:00:00–11:00:00 LT), midday (11:00:00–13:00:00 LT), and afternoon  
 270 (13:00:00–17:00:00 LT) approaches at Don Mueang International Airport, whose location relative to the Bangkok urban plume  
 271 is shown in (c).

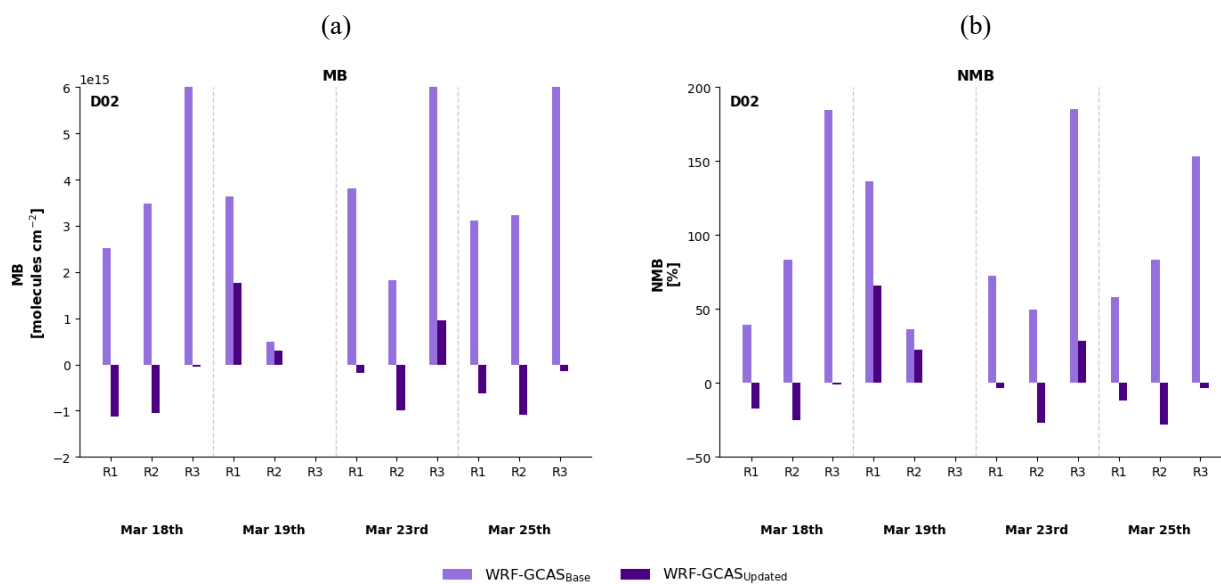


284

285 **Figure S19.** Spatial comparison over the BMR on 18 March 2024 of tropospheric NO<sub>2</sub> columns from (a) GCAS, (b) WRF-

286 GCAS<sub>Updated</sub> D01, and (c) WRF-GCAS<sub>Base</sub> D01 for raster periods corresponding to morning, midday, and afternoon local time.

287



289

290 **Figure S20.** (a) Mean bias (MB) and (b) normalized mean bias (NMB) comparing WRF-GCAS<sub>Base</sub> D02 (light purple) and  
 291 WRF-GCAS<sub>Updated</sub> D02 (dark purple) against GCAS observations for each raster period and ASIA-AQ flight day. Bias  
 292 reductions in WRF-GCAS<sub>Updated</sub> D02 increase throughout the day, indicating improved representation of the daytime NO<sub>2</sub>  
 293 evolution relative to the base simulation.

294

295

296

297

298

299

300

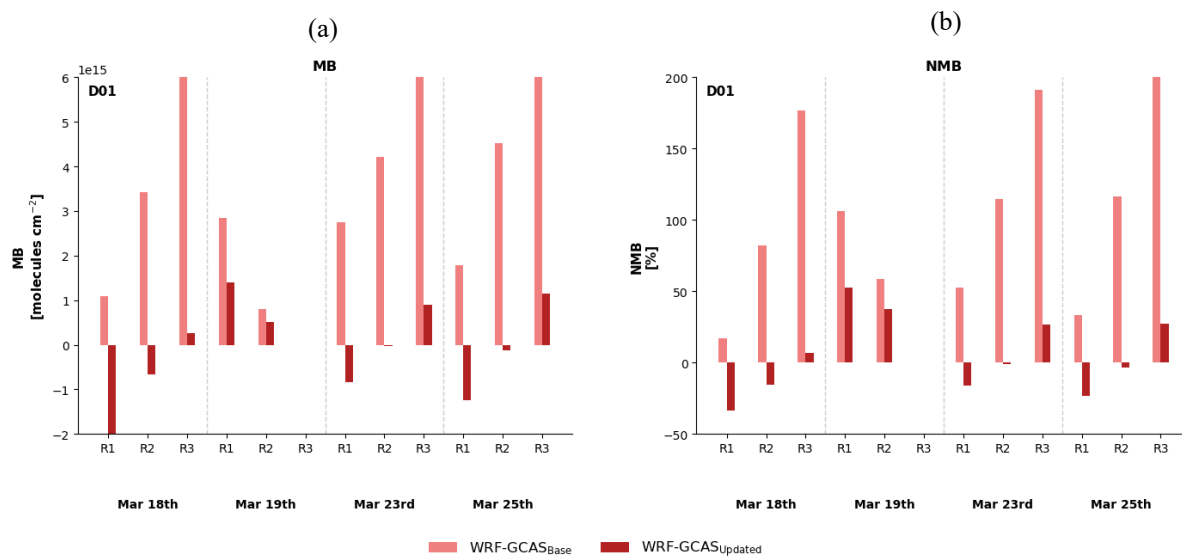
301

302

303

304

305



306

307 **Figure S21.** (a) Mean bias (MB) and (b) normalized mean bias (NMB) comparing WRF-GCAS<sub>Base</sub> D01 (light red) and WRF-  
 308 GCAS<sub>Updated</sub> D01 (red) against GCAS observations for each raster period and ASIA-AQ flight day. Bias reductions in WRF-  
 309 GCAS<sub>Updated</sub> D01 increase throughout the day, indicating improved representation of the daytime NO<sub>2</sub> evolution relative to the  
 310 base simulation.

311

312

313

314

315

316

317

318

319

320

321

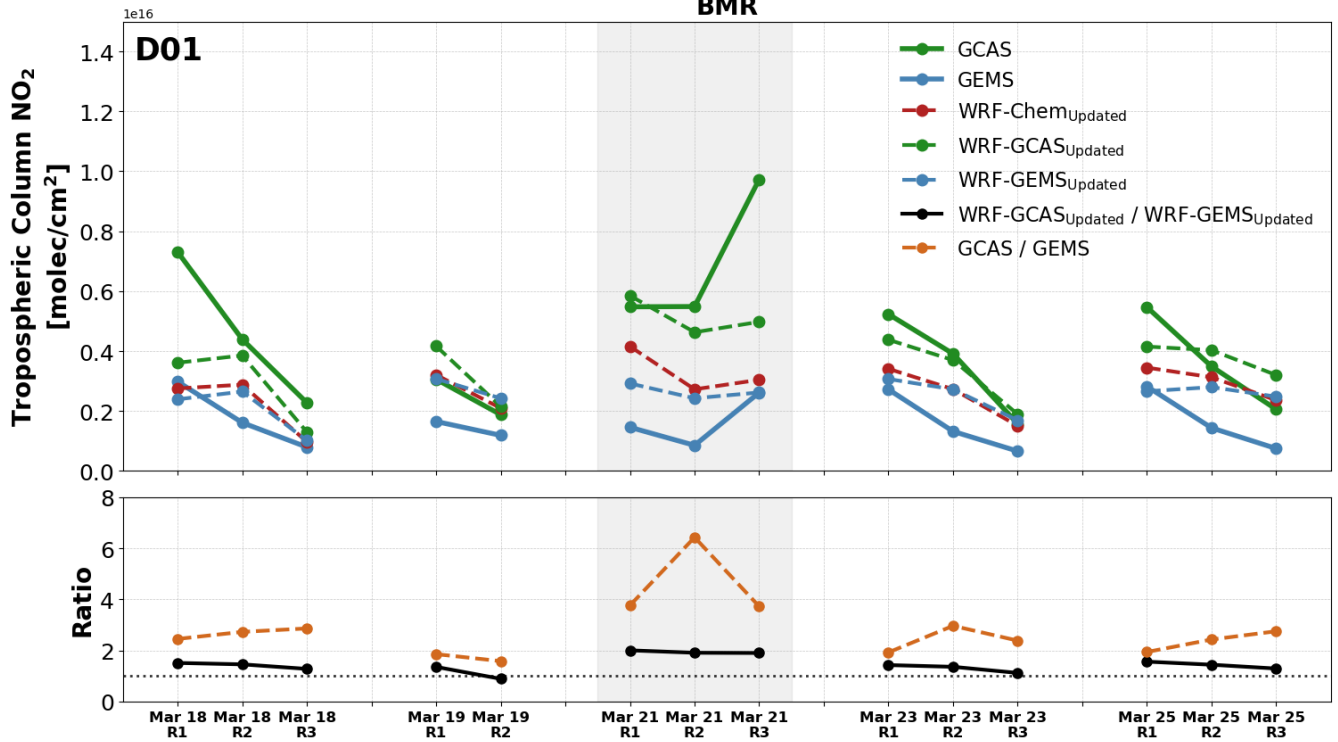
322

323

324

325

## NO<sub>2</sub> Column Raster Evaluation BMR



326

327

**Figure S22.** Daily raster comparison of tropospheric NO<sub>2</sub> columns from WRF<sub>Updated</sub> D01 (dashed red), WRF-GCAS<sub>Updated</sub> D01 (dashed green), WRF-GEMS<sub>Updated</sub> D01 (dashed blue), GCAS (green), and GEMS (blue) for ASIA-AQ flight days. Dashed model lines indicate simulations with instrument-specific averaging kernels applied. The difference in sensitivity between GCAS and GEMS measurements is illustrated by the ratio of WRF-GCAS to WRF-GEMS, plotted in black.

331

332

333

334

335

336

337